

See discussions, stats, and author profiles for this publication at: <https://www.researchgate.net/publication/261031224>

Carbon Pipette-Based Electrochemical Nanosampler

ARTICLE *in* ANALYTICAL CHEMISTRY · MARCH 2014

Impact Factor: 5.64 · DOI: 10.1021/ac403547b · Source: PubMed

CITATIONS

7

READS

57

7 AUTHORS, INCLUDING:



[Yun Yu](#)

CUNY Graduate Center

11 PUBLICATIONS 47 CITATIONS

[SEE PROFILE](#)



[Olha Mashtalir](#)

Drexel University

20 PUBLICATIONS 556 CITATIONS

[SEE PROFILE](#)



[Gary Friedman](#)

Drexel University

228 PUBLICATIONS 5,326 CITATIONS

[SEE PROFILE](#)



[Yury Gogotsi](#)

Drexel University

628 PUBLICATIONS 26,571 CITATIONS

[SEE PROFILE](#)

Carbon Pipette-Based Electrochemical Nanosampler

Yun Yu, Jean-Marc Noël,[†] and Michael V. Mirkin*

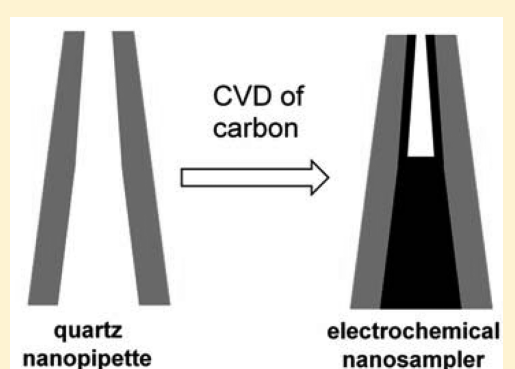
Department of Chemistry and Biochemistry, Queens College—CUNY, Flushing, New York 11367, United States

Yang Gao,^{†,§} Olha Mashtalir,^{‡,§} Gary Friedman,^{†,§} and Yury Gogotsi*,^{‡,§}

[†]Department of Electrical and Computer Engineering, [‡]Department of Materials Science and Engineering, and [§]A.J. Drexel Nanotechnology Institute, Drexel University, 3141 Chestnut Street, Philadelphia, Pennsylvania 19104, United States

Supporting Information

ABSTRACT: Sampling ultrasmall volumes of liquids for analysis is essential in a number of fields from cell biology to microfluidics to nanotechnology and electrochemical energy storage. In this article, we demonstrate the possibility of using nanometer-sized quartz pipettes with a layer of carbon deposited on the inner wall for sampling attoliter-to-picoliter volumes of fluids and determining redox species by voltammetry and coulometry. Very fast mass-transport inside the carbon-coated nanocavity allows for rapid exhaustive electrolysis of the sampled material. By using a carbon pipette as the tip in the scanning electrochemical microscope (SECM), it can be precisely positioned at the sampling location. The developed device is potentially useful for solution sampling from biological cells, micropores, and other microscopic objects.



Advances in nanoelectrochemistry made over the last two decades^{1,2} provided new tools for electrochemical experiments in ultrasmall (pico- to zeptoliter) volumes.^{3–6} In addition to fundamentally interesting physicochemical measurements at the level of single molecules,^{7–9} such experiments can offer important advantages for cell biology,^{10–12} microfluidics,¹³ and nanotechnology.¹⁴ The two alternative strategies for these experiments are either to take measurements *in situ* (e.g., inside a biological cell^{3,6} or a vesicle⁵) or to sample solution for subsequent analysis (e.g., in a picoliter vial¹⁵). The former approach may be more straightforward, but not always feasible, whereas the latter requires a suitable tool for solution sampling and transfer.

The sampling devices are often plagued by the common problem, a relatively large tip size. Additionally, the sampled solution must not be significantly diluted or contaminated before the analysis. For example, the contamination and alteration of a sample was a potential issue with the “attosyringe”, a nanopipette-based device, which we previously employed for solution sampling and intracellular injections: organic solvent contained inside the pipette could damage the sampled biomolecules.¹⁶ The electrochemical nanosampler discussed in this paper is free from both problems. It is produced by chemical vapor deposition (CVD) of a thin carbon layer on the inner surface of a quartz pipette whose tip radius can be as small as a few nanometers.¹⁷ The resulting geometry is shown schematically in Figure 1. When a nanosampler is placed in either aqueous or organic solution, a small volume of liquid gets driven into the carbon-coated nanopipette (CNP)

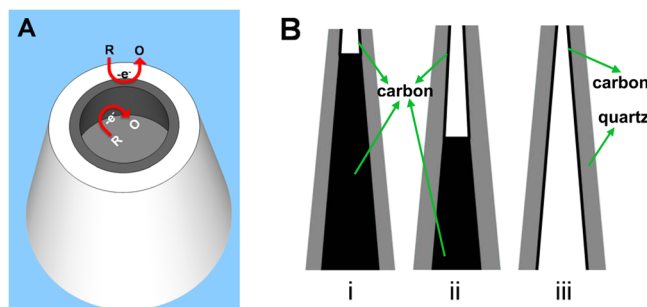


Figure 1. Schematic representation of an electrochemical nanosampler. (A) Oxidation of redox active species (R) occurs on the carbon-coated inner pipette wall and on the carbon nanoring exposed to solution. (B) Nanosampler behavior depends on the depth of its cavity: (i) shallow, (ii) relatively deep, and (iii) very deep (open CNP).

by capillary forces. The redox species contained in solution (e.g., the reduced form, R, pictured in Figure 1A) can be oxidized or reduced at the carbon nanoring exposed to external solution and at the carbon surface inside the pipette. The voltammetric response of such an electrode should include a steady-state component produced by the convergent diffusion and a transient component due to the oxidation/reduction of

Received: November 2, 2013

Accepted: March 11, 2014

Published: March 21, 2014



the sampled redox species inside the pipette. The shape of the resulting voltammograms strongly depends on the depth of the carbon nanocavity, which can be either shallow (i.e., the depth is equivalent to a few pipette radii; panel i in Figure 1B), deep (Figure 1B, panel ii), or essentially infinite (open carbon pipette in Figure 1B, panel iii). It is shown below that each geometry is suitable for rapid exhaustive electrolysis of the sampled species due to the very fast mass-transfer inside the nanopipette.

EXPERIMENTAL SECTION

Chemicals. Ferrocenemethanol (FeMeOH; 99%, Alfa Aesar) was sublimed before use. Hexaammineruthenium(III) chloride (99%, Strem Chemicals) was used as received. Aqueous solutions were prepared from deionized water (Milli-Q, Millipore Corp.), and KCl (99+, Sigma-Aldrich) was used as the supporting electrolyte.

Fabrication of Carbon Nanopipettes. Quartz capillaries (1.0 mm o.d., 0.3 mm i.d. and 1.0 mm o.d., 0.7 mm i.d.) were purchased from Sutter Instrument Co. The nanopipettes with the tip diameter from 10 to 200 nm were pulled by a laser pipette puller (P-2000; Sutter Instruments) from these quartz capillaries. A layer of carbon was deposited inside the quartz pipette by the CVD method, using methane as the carbon source and argon as the protector, as described previously.¹⁷ The Ar flow of 200 standard cubic centimeters per minute (scm) was passed through the CVD reaction chamber during heating. Once the furnace temperature reached 875 °C, a mixed flow of methane and Ar was passed through the reaction chamber.

Different types of carbon nanopipettes were fabricated by controlling the CVD time and the composition of the gas mixture. A relatively short CVD time (30 min) and lower methane to argon ratio yielded the pipettes with an open path in the middle (panel iii in Figure 1B). Conversely, by increasing CVD time to ≥90 min and using a higher methane to argon ratio, one can increase the carbon layer thickness and close the path, leaving a cavity at the very end of tapered shaft (panels i and ii in Figure 6B). In this study, the CVD time of 100 min and the 1:1 methane to argon ratio produced nanoelectrodes with carbon layers on the inner wall of the quartz pipette that blocked the pipette channel and contained a cavity adjacent to the end of the capillary. Cavity depth can be equivalent to ~4 to ~200 pipette radii depending on tip diameter and pipette geometry. Several other factors, including the furnace temperature and total gas flow rate, can also affect the synthesized carbon layer morphology.

Characterization of Nanopipettes by SEM and TEM. A Zeiss Supra 50VP scanning electron microscope (SEM) was used to characterize surface morphology of the fabricated nanoelectrodes. The side view of the tip was used to verify the absence of a carbon layer on the outer wall formed during CVD, and the top view showed the size of the nanopipette orifice. Side view images were taken with the 1.5–3 kV gun voltage and top view images with 1.5–2 kV voltage for a typical working distance of 4 mm. A JEOL JEM-2100 transmission electron microscope (TEM) was used to characterize the carbon distribution near the tip of the nanopipette. The pipette was attached to the grid (PELCO Hole Grids, Copper) in such a way that its tip was shown in the grid center hole, and the rest of the pipette was cut off. A relatively low electron beam voltage of 120 kV was used to reduce charge/heat accumulating effects on the glass layer. The TEM images showed that under

different carbon deposition conditions the pipettes could either have an open path in the middle or a nanocavity at the tip.

Electrochemical Experiments. The two-electrode setup was used with a 0.25 mm diameter Ag wire coated with AgCl serving as a reference electrode. Voltammograms were obtained using a BAS-100B electrochemical workstation (Bioanalytical Systems, West Lafayette, IN). All experiments were carried out at room temperature (22–25 °C) inside a Faraday cage.

SECM Setup. SECM experiments were carried out using a home-built instrument, which was similar to that described previously.¹⁸ A clean silanized glass slide was used as the substrate in negative feedback experiments. To obtain an SECM approach curve, the nanosampler used as a tip was first positioned a few hundred micrometers above the substrate surface. To avoid crashing, this process was monitored with a long-distance video microscope. Then, the tip was moved closer to the substrate in the automated “surface hunter” mode until the tip current produced by oxidation of FcMeOH decreased by ~10%. The tip current was collected during the subsequent fine approach.

Finite Element Simulations. The electrochemical response of the carbon-coated nanopipette was modeled for a Nernstian one-electron redox process assuming diffusion-controlled mass-transport (excess supporting electrolyte). The time-dependent and steady-state voltammetric responses were simulated using COMSOL Multiphysics v4.2a (Comsol, Inc.). The axisymmetric diffusion problem for the nanosampler geometry is shown in the Appendix, and the COMSOL Model Report describing the simulation can be found in the Supporting Information.

RESULTS AND DISCUSSION

Electrochemical Nanosampler Geometry. Deposition of carbon inside quartz nanopipettes has been studied extensively. TEM and optical studies of the films inside pipettes and electrical conductivity measurements showed that films are continuous and, under the selected deposition conditions, carbon spreads from the tip through the entire length of the pipette.^{17b} The geometry of a CNP is defined by several parameters: the orifice radius, a , the radius of outer wall, r_g , the tip taper angle, θ , and the depth of the carbon-coated cavity, h (Figure 2). For quartz pipettes used in our experiments, the typical value of the dimensionless parameter, $RG = r_g/a$ is 1.5–2.^{17c,18} The cavity depth effect depends on the value of another dimensionless parameter, $H = h/a$. The orifice radius, a , can be evaluated from steady-state voltammetry, and the thickness of the carbon layer at the tip does not considerably affect the

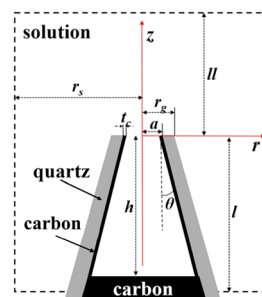


Figure 2. Parameters defining the diffusion problem for a CNP and the geometry of the simulation space.

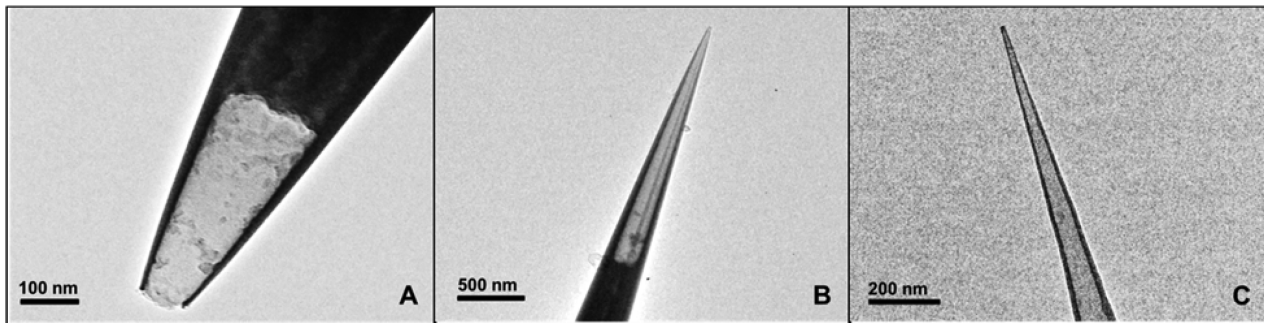


Figure 3. TEM images of carbon coated nanopipettes with different cavity depths. (A) $a = 33 \text{ nm}$, $\theta = 8^\circ$, $H = 12$; (B) $a = 10 \text{ nm}$, $\theta = 5^\circ$, $H = 190$; (C) open pipette, $a = 4 \text{ nm}$, $\theta = 2^\circ$.

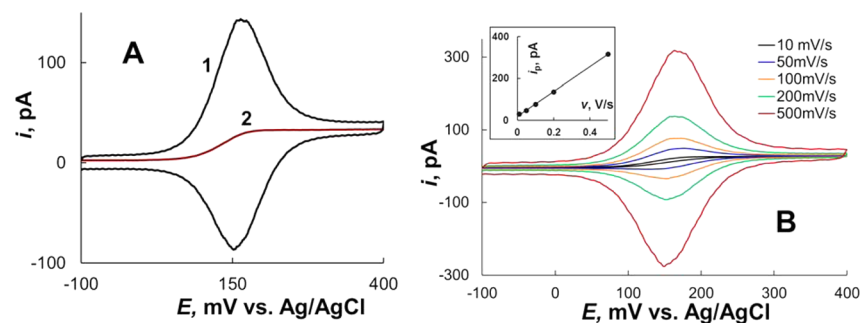


Figure 4. CVs of 1 mM FeMeOH in 0.2 M KCl solution obtained using an $\sim 100 \text{ nm}$ radius CNP at different potential sweep rates. (A) $v = 200 \text{ mV/s}$ (1) and 10 mV/s (2). (B) A family of curves obtained for the range of v from 10 to 500 mV/s. The inset shows the dependence of the anodic peak current on v .

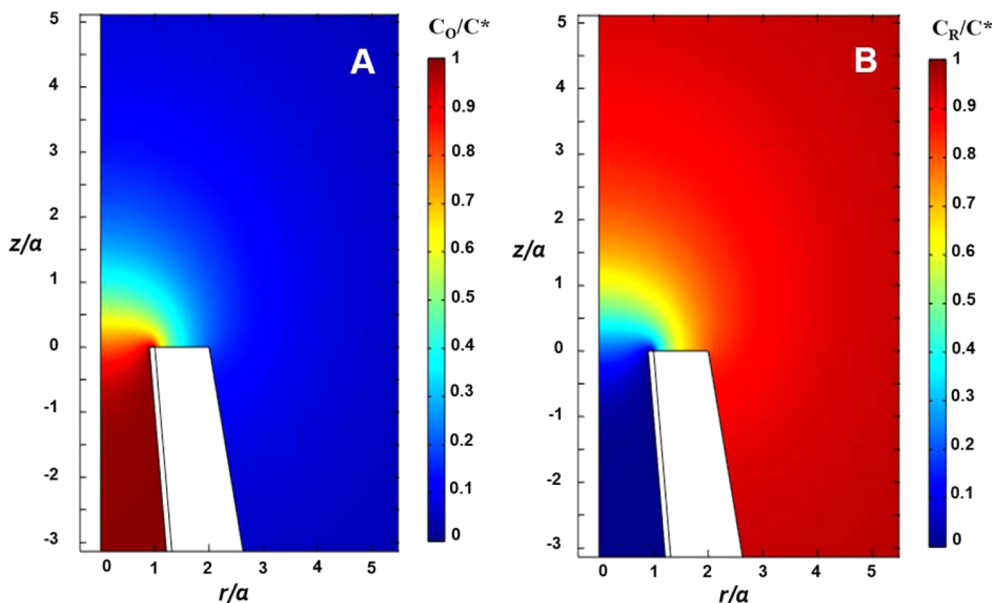


Figure 5. Portions of simulated concentration profiles of (A) oxidized and (B) reduced species adjacent to the pipette orifice at a positive potential corresponding to diffusion limiting current. $E = E^{\circ'} + 200 \text{ mV}$, $H = 50$, $\tan \theta = 0.1$.

electrochemical response as long as it is significantly smaller than a (e.g., $\leq 0.2a$; see below).

The geometric parameters of the pipette, i.e., a , h , and θ , can be evaluated from TEM and SEM images. Figure 3 shows TEM images of pipettes with the carbon coated inner wall, corresponding to three cases shown schematically in Figure 1B, i.e., with a shallow nanocavity (Figure 3A), relatively deep cavity (Figure 3B), and a carbon pipette with an open path

(Figure 3C). The volume of the cavity filled with solution can also be evaluated coulometrically (see below).

Voltammetric Response of the Nanosampler: Experiments and Simulations. A typical cyclic voltammogram (CV) of FeMeOH at a carbon-coated nanopipette electrode (curve 1 in Figure 4A) exhibits an unusual combination of the steady-state plateau current at extreme positive potentials with a pair of prominent slightly asymmetrical peaks. From the

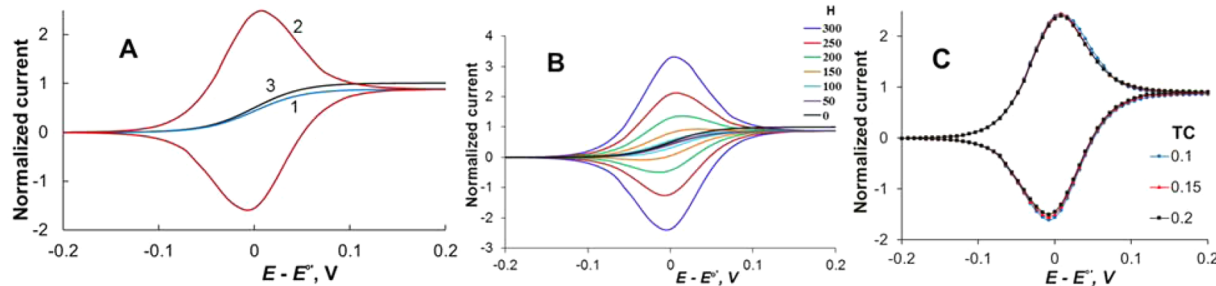


Figure 6. Simulated voltammetric responses of CNP electrodes. (A) CNP voltammograms at slow (1; $\sigma = 10^{-7}$) and fast (2; $\sigma = 10^{-2}$) scan rates, $H = 50$; a steady-state voltammogram at the inlaid disk electrode (3). (B) Effect of the cavity depth (H) on the shape of CNP voltammograms. $\sigma = 10^{-4}$. (C) Effect of the carbon layer thickness ($TC = t_c/a$) on the shape of CNP voltammograms. $\sigma = 10^{-2}$; $H = 50$.

diffusion limiting steady-state current, the effective radius $a = 100$ nm can be evaluated using eq 1 for an inlaid disk (see below)

$$i_d = 4xnFDc^*a \quad (1)$$

where $n = 1$ is the number of transferred electrons, F is the Faraday constant, $c^* = 1$ mM and $D = 7.6 \times 10^{-6}$ cm²/s¹⁹ are the bulk concentration and the diffusion coefficient of FcMeOH, respectively. The factor x is a function of RG;²⁰ $x = 1.1$ corresponds to RG = 2.0, which is typical of thick-wall quartz pipettes used in this study.

The appearance of two peaks with the potentials close to the formal potential of FcMeOH (E°') in the nanoelectrode CV obtained at a relatively slow potential sweep rate (e.g., $v \geq 50$ mV/s in Figure 4B) is indicative of the thin layer cell (TLC) type behavior. Such a response can be attributed to complete oxidation of FcMeOH molecules inside the carbon-coated pipette shaft during the anodic potential scan and subsequent reduction of ferrocenium species during the reverse cathodic scan. Unlike regular twin-electrode TLCs,²¹ the peaks in Figure 4A are slightly asymmetrical and the forward (anodic) peak is somewhat higher than the reverse one. This shape results from the addition of the steady-state diffusion current to the pipette orifice (curve 2 in Figure 4A) to both anodic and cathodic portions of a symmetrical TLC (which represent the oxidation and reduction of the redox mediator inside the pipette, respectively). The addition of the steady-state anodic component makes the anodic peak in curve 1 somewhat higher and the cathodic peak lower.

The CV shape depends greatly on the potential sweep rate. Curve 2 in Figure 4A obtained at low $v = 10$ mV/s is completely sigmoidal and can hardly be distinguished from a steady-state voltammogram obtained at a flat disk nanoelectrode. In contrast, a faster scan CV (curve 1 in Figure 4A; $v = 200$ mV/s) is peak-shaped. As expected for TLCs,²¹ the peak current measured with carbon-coated nanopipettes is directly proportional to v (see the inset in Figure 4B), while the steady-state current due to the quasi-spherical diffusion to the carbon nanoring in the external solution is essentially independent of v (Figure 4B). The charging current is somewhat higher than that obtained with typical nanoelectrodes due to the larger carbon/solution interface inside the CNP.

The voltammetric features in Figure 4 are in agreement with the results of finite element simulations (Figures 5 and 6). Simulated concentration profiles of oxidized (Figure 5A) and reduced (Figure 5B) forms of FcMeOH at $E = E^\circ' + 200$ mV consist of two distinct parts, a quasi-spherical diffusion layer

near the pipette orifice with the radius comparable to a and the entire carbon-coated nanocavity in which all FcMeOH species are oxidized. These two parts of the diffusion field are responsible for the steady-state and time-dependent components of the electrode response in Figure 4.

The shapes of the simulated CVs (Figure 6) are very similar to those of the experimental curves in Figure 4. When the dimensionless scan rate, $\sigma = (a^2/4D)(nFv/RT)$ is small, sigmoidal and retraceable voltammograms (e.g., curve 1 in Figure 6A) suggest that the non-steady-state current inside the pipette completely vanishes on this relatively long experimental time scale ($\sigma = 10^{-7}$ corresponds to $v = 5$ mV/s if $a = 50$ nm). The shape of curve 1 and the diffusion limiting current value are quite similar to those computed for a disk electrode of the same radius (curve 3 in Figure 6A). One can compare the steady-state response of the CNP to that of the inlaid ring electrode.²² The diffusion current is slightly higher in the former case because the redox species penetrating inside the pipette shaft get quickly oxidized (or reduced) at the carbon-coated inner wall. For instance, with the carbon layer thickness $t_c = 0.1a$, the diffusion limiting steady-state current at the CNP is ~88% of that to the disk electrode of the same radius (eq 1); this is somewhat higher than the ~81% value calculated for the inlaid ring electrode with the same ring thickness and radius.²²

At a fast scan rate, the simulated CV (curve 2 in Figure 6A) exhibits a pair of prominent peaks corresponding to oxidation and reduction of the redox species in the nanocavity inside the CNT. The rapid mass-transfer in the nanocavity results in exhaustive electrolysis of sampled molecules even on a short experimental time scale ($\sigma = 10^{-2}$ corresponds to $v = 500$ V/s if $a = 50$ nm), and at $E \gg E^\circ'$, the anodic current decreases to the steady-state value, which is independent of v (cf. curves 1 and 2 in Figure 6A).

The family of simulated CVs in Figure 6B illustrates the effect of the cavity depth on the nanosampler response at a constant scan rate ($\sigma = 10^{-4}$). With increasing H , the transition can be seen from the steady-state behavior of an inlaid disk ($H = 0$) to peak-shaped CVs. At moderate scan rates, the peaks are observable only if $H \gg 1$ (e.g., $H \geq 50$ in Figure 6B) because the total charge of molecules undergoing oxidation/reduction is directly proportional to the nanocavity volume. At smaller H , the recorded steady-state voltammograms are very similar to those obtained at an inlaid disk except for a slightly lower plateau current. Neither a steady-state nor a time-dependent component of the voltammetric current depends strongly on the thickness of the carbon layer as long as $TC \ll 1$ (Figure 6C).

The steady-state diffusion limiting current in Figure 6B is essentially independent of the cavity depth, in sharp contrast with recessed nanoelectrodes²³ or nanopore electrodes,²⁴ where it decreases markedly when $H \gg 1$. This difference is due to the conductive carbon ring on the edge of the CNP orifice. Figure 7 contrasts the shapes of CVs simulated for

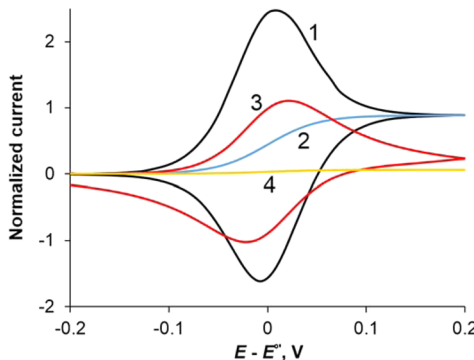


Figure 7. Simulated CVs for a CNP (curves 1 and 2) and a recessed disk electrode (curves 3 and 4) with the same normalized cavity depth, $H = 50$. $\sigma = 10^{-2}$ (1, 3) and 10^{-7} (2, 4).

CNPs (curves 1 and 2) and recessed disk electrodes (curves 3 and 4). At the faster scan rate ($\sigma = 10^{-2}$), curve 1 exhibits a pair of TLC-like peaks with the height proportional to v and a very small peak separation due to the exhaustive electrolysis inside the CNP. The CV symmetry is somewhat distorted by the contribution of the steady-state oxidation current. In contrast, curve 3 with asymmetrical diffusion peaks separated by ~ 50 mV is similar to the Nernstian CV at the infinite planar electrode²⁵ due to essentially linear diffusion inside the conical pore of a deeply recessed electrode.²⁴ The difference in CV shape stems from the presence of the conductive carbon layer on the inner pipette wall, which results in the fast mass-transfer rate inside a deep nanocavity. At a slow scan rate, the ($\sigma = 10^{-7}$), the steady-state CNP voltammogram (curve 2) is strikingly different from essentially flat curve 4 calculated for a deeply recessed disk ($H = 50$).

A CNP with an open path in the middle can also be used for sampling solution species. The CVs obtained with open CNPs (Figure 8A) are similar to those at CNP electrodes with a finite cavity volume (Figure 8B). The difference is that in the latter case subsequent cyclic scans are essentially identical, while in the former the current increases with the scan number due to the gradual advance of the solution front into the “infinitely” long pipette shaft.

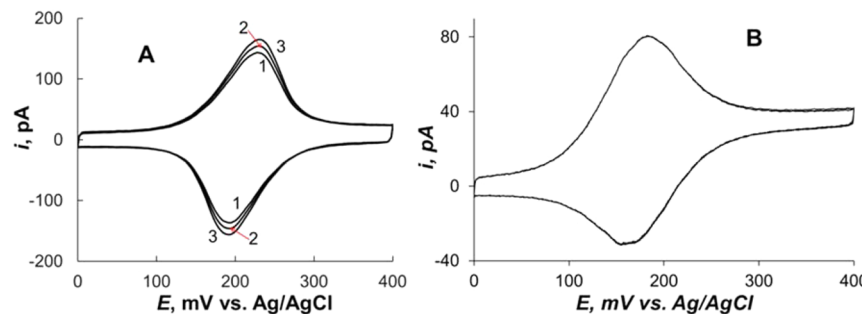


Figure 8. Three consecutive cyclic voltammometric scans obtained using an open CNP (A) and a CNP with a finite cavity (B) in 0.2 M KCl aqueous solution containing 1 mM FcMeOH. $v = 100$ mV/s. The cycle numbers are shown in A. a , nm = 46 (A) and 115 (B).

Coulometry of Sampled Molecules. The number of redox molecules sampled inside a CNP can be found by integrating their oxidation or reduction current. For accurate analysis, the contribution of the steady-state diffusion current from the external solution and the double layer charging current have to be subtracted. Two slightly different situations are shown in Figure 9. At a relatively slow scan rate (e.g., 500

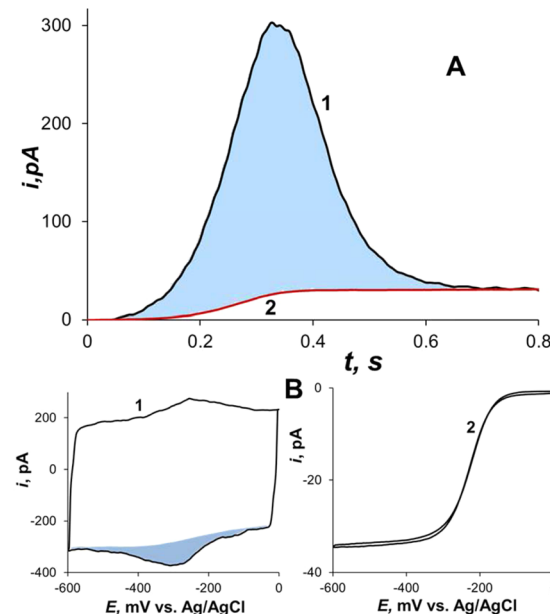


Figure 9. Evaluation of the amount of analyte in the nanocavity from CNP voltammograms. (A) Voltammetric responses of a 100 nm radius CNP in 0.2 M KCl aqueous solution containing 1 mM FcMeOH. v , mV/s = 500 (1) and 10 (2). (B) CNP CVs of 40 mM Ru(NH₃)₆Cl₃ in 0.5 M KCl. v , V/s = 50 (1) and 0.05 (2). a = 3 nm.

mV/s; curve 1 in Figure 9A) and a deep cavity, the charging current is less important, but the steady-state component can be significant. The colored area under the peak and above the steady-state curve (Figure 9A) corresponds to the charge, $Q_{Fc} = 5.7 \times 10^{-11}$ C and $N_{Fc} = 5.9 \times 10^{-16}$ mol of FcMeOH sampled in the cavity.

At a much higher v (e.g., 50 V/s; curve 1 in Figure 9B), the contribution of the charging current is more significant than the steady-state component (curve 2 in Figure 9B; $v = 50$ mV/s). The charge value found after the subtraction is $Q_{Fc} = 4.7 \times 10^{-13}$ C, corresponding to $N_{Fc} = 4.9 \times 10^{-18}$ mol of FcMeOH in the cavity. These numbers are much smaller than those found from Figure 9A because the CNP used in Figure 9B was

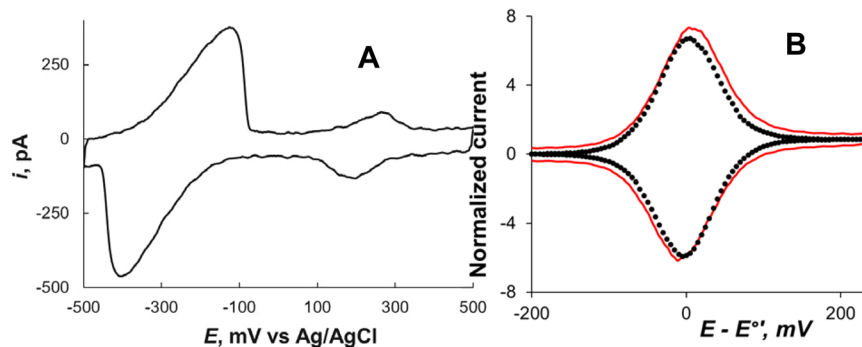


Figure 10. Evaluation of the analyte concentration and nanocavity volume from CNP voltammograms. (A) Voltammetric response of an ~ 30 nm radius CNP in 0.2 M KCl aqueous solution containing 1 mM FcMeOH and 7 mM $\text{Ru}(\text{NH}_3)_6\text{Cl}_3$. $v = 10$ V/s. (B) Experimental (solid line) and simulated (symbols) CVs of 1 mM FcMeOH in 0.2 M KCl at a 140 nm radius CNP. $v = 500$ mV/s. Simulation parameters: RG = 1.8, H = 298, $\tan \theta = 0.08$.

very small; $a = 3$ nm was calculated from the steady-state current in curve 2. The cavity volume, $V = (Q_{\text{Fc}}/\text{Fc}_{\text{Fc}}^*) = 1.2 \times 10^{-16} L = 120 \text{ aL}$ was calculated from curve 1. This attoliter volume is comparable to the amount of liquid trapped in a single nanotube.²⁶

Although the number of sampled redox species can be evaluated from the integrated current without any information about CNP geometry, to determine the concentration of redox species from CNP coulometry, one needs to know the volume of the sampled solution. This quantity is not easily accessible, but it can be determined by adding to the solution a known concentration of the second redox species to be used as a standard. The nanosampler calibration is illustrated by Figure 10, which shows a voltammogram obtained in a 0.2 M KCl solution containing 1 mM FcMeOH and the “unknown” concentration of $\text{Ru}(\text{NH}_3)_6^{3+}$ (7.0 mM). From the pair of FcMeOH oxidation/reduction peaks (the midpoint potential ~ 230 mV vs Ag/AgCl; the difference between the anodic and cathodic peak potentials is due to the resistive potential drop inside the CNP), one can find the total charge of oxidation of FcMeOH within the cavity, $Q_{\text{Fc}} = 0.83 \text{ pC}$. This corresponds to the cavity volume, $V = 8.6 \times 10^{-12} \text{ cm}^3 = 8.6 \text{ fL}$. The charge equivalent to the complete reduction of $\text{Ru}(\text{NH}_3)_6^{3+}$ within the same cavity is $Q_{\text{Ru}} = 5.8 \text{ pC}$, and the concentration of this species can be evaluated as

$$c_{\text{Ru}}^* = \frac{c_{\text{Fc}}^* Q_{\text{Ru}}}{Q_{\text{Fc}}} = 6.9 \text{ mM} \quad (2)$$

in good agreement with the actual value of 7.0 mM.

The cavity volume value can also be validated by fitting an experimental CV to the theory (Figure 10B). Minor differences between the experimental and simulated curves in Figure 10B are caused by the charging current and resistive potential drop inside the CNP, which are not included in our simulations. From the experimental CV, the current integration under the anodic peak yields the charge associated with the oxidation of sampled FcMeOH, $Q_{\text{Fc}} = 57 \text{ pC}$. With the FcMeOH concentration of 1 mM, this charge corresponds to $V = 0.59 \text{ pL}$. The 0.55 pL cavity volume calculated for the geometry used in the simulation ($a = 140$ nm, $h = 298a$, and $\tan \theta = 0.08$) agrees well with the experimental value.

CNP as an SECM Tip. Precise positioning of a CNP is necessary to enable solution sampling from small spaces. This is hard to achieve because the nanosampler tip is too small to be seen by optical microscopy. One needs nanoscale positioning

precision to insert such a probe inside a submicrometer-sized vesicle or a microscopic pore in a catalyst layer. Precise positioning and nanoscale motion control in penetration experiments have previously been attained by using a nanoelectrode as an SECM tip.^{6,16,27} Because the redox species reaching the CNP orifice by diffusion are quickly oxidized (or reduced) either at the carbon nanoring exposed to external solution or at the portion of the conductive inner wall adjacent to the aperture, the CNP steady-state response is quite similar to that of the inlaid disk electrode (cf. curves 1 and 3 in Figure 6A). Expectedly, the shapes of SECM approach curves obtained with a CNP tip were in agreement with the theory for a disk-shaped tip. An SECM current vs distance curve obtained with a CNP tip approaching an insulating glass substrate (Figure 11) was fitted to the theory for the negative feedback (black line),²⁸ using RG = 2 and the radius value, $a = 98$ nm, calculated from the diffusion limiting current.

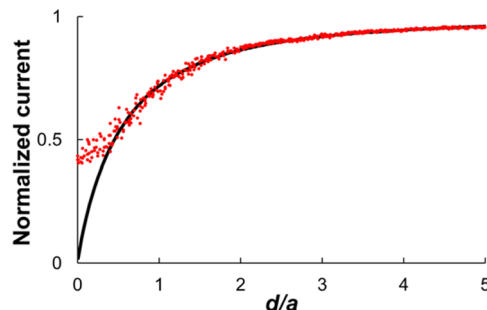


Figure 11. SECM current-distance curve obtained with a CNP tip approaching an insulating glass substrate (symbols) and corresponding theory for the pure negative feedback (solid line; RG = 2).²⁸ The current and distance are normalized by $i_{T,\infty} = 28 \text{ pA}$ and $a = 98 \text{ nm}$, respectively. Solution contained 1 mM FcMeOH and 0.1 M KCl.

Although an unpolished CNP is not a perfect SECM tip, the fit between the theory and experiment in Figure 11 is sufficiently good to establish the distance scale and facilitate the positioning of the nanosampler in a close proximity of the substrate.

Another potential advantage of the nanosampler is a higher sensitivity—the signal produced by oxidation/reduction inside a CNP can be significantly higher than the steady-state current to the orifice of the same pipette (Figure 4B). The work is underway in our laboratories to modify the CNP inner surface and, thus, produce sensors for species that cannot be measured

at carbon electrodes. For instance, a sensor for sampling reactive oxygen and nitrogen species can be produced by depositing Pt black inside the nanocavity.^{17c}

One should notice that the diffusion of species from the outer solution into the pipette and back is relatively slow. Thus, rapid changes in the composition of the outer solution (e.g., near a biological cell surface) would affect the steady-state current to the carbon ring rather than the transient current produced by the oxidation/reduction inside the CNP. By the same reason, no significant loss of the sampled species can be caused by their diffusion away from the cavity.

CONCLUSIONS

We presented a new technique for sampling small volumes (attoliter to picoliter) of solution and rapid electrochemical analysis of sampled redox species. The electrochemical nanosampler can be useful when direct electrochemical measurements are difficult, e.g., in biological vesicles and other subcellular compartments, in catalysis nanopores, and inside working batteries or fuel cells. We simulated voltammetric responses of the nanosampler, a carbon filled quartz pipette with a nanocavity inside, and demonstrated good agreement between simulated and experimental CVs. Exhaustive electrolysis of sampled redox species results in measurable oxidation/reduction peaks at moderate potential sweep rates if the nanocavity depth is much larger than its radius (e.g., $H \geq 50$). The faster the sweep rate the smaller the lower limit for the cavity volume; however, excessively high capacitive charging current at very high v may hinder the use of extremely small CNPs with shallow cavities.

To facilitate precise positioning of the nanosampler near the object of interest, it can be used as an SECM probe. Experimental approach curves obtained with a CNP tip can be quantitatively fit to the theory to establish the distance scale and control the probe position relative to the sample.

APPENDIX

Time-Dependent Diffusion Problem for the Electrochemical Nanosampler

The diffusion problem for the electrochemical nanosampler is formulated here for reduced species (R) and excess supporting electrolyte initially present in solution. The corresponding differential equations in cylindrical coordinates are the following:

$$\frac{\partial c_R}{\partial t} = D_R \left(\frac{\partial^2 c_R}{\partial r^2} + \frac{1}{r} \frac{\partial c_R}{\partial r} + \frac{\partial^2 c_R}{\partial z^2} \right) \quad (\text{A1})$$

$$\frac{\partial c_O}{\partial t} = D_O \left(\frac{\partial^2 c_O}{\partial r^2} + \frac{1}{r} \frac{\partial c_O}{\partial r} + \frac{\partial^2 c_O}{\partial z^2} \right) \quad (\text{A2})$$

where t is time, r and z are the coordinates in directions parallel and normal to the pipette orifice plane, respectively; $c_R(r, z, t)$ and $c_O(r, z, t)$ are the concentrations of R and O species, respectively; D_R and D_O are the diffusion coefficients of R and O species, respectively. In this article, $D_R = D_O = D$. The normalized dimensionless variables can be introduced as follows:

$$R = \frac{r}{a} \quad (\text{A3.a})$$

$$Z = \frac{z}{a} \quad (\text{A3.b})$$

$$C_O(R, Z, \tau) = \frac{c_O(r, z, t)}{c^*}, C_R(R, Z, \tau) = \frac{c_R(r, z, t)}{c^*} \quad (\text{A3.c})$$

$$\text{LL} = \frac{l l}{a} \quad (\text{A3.d})$$

$$L = \frac{l}{a} \quad (\text{A3.e})$$

$$\text{RG} = \frac{r_g}{a} \quad (\text{A3.f})$$

$$\text{RS} = \frac{r_s}{a} \quad (\text{A3.g})$$

$$H = \frac{h}{a} \quad (\text{A3.h})$$

$$\text{TC} = \frac{t_c}{a} \quad (\text{A3.i})$$

$$\tau = \frac{4Dt}{a^2} \quad (\text{A3.j})$$

where c^* is the bulk concentration of R in the solution, r_g is the insulator radius, r_s is the simulation space limit in the radial direction, ll and l are the z coordinates of the upper and lower simulation space limits, respectively; h is the recess depth, and t_c is the carbon layer thickness. The oxidation current at the carbon surface was calculated by solving the following diffusion problem in the dimensionless form:

$$\frac{\partial C_R}{\partial \tau} = \frac{\partial^2 C_R}{\partial R^2} + \frac{1}{R} \frac{\partial C_R}{\partial R} + \frac{\partial^2 C_R}{\partial Z^2}; \quad \tau > 0, 0 \leq R < \text{RS}, -L < Z < \text{LL} \quad (\text{A4.a})$$

$$\frac{\partial C_O}{\partial \tau} = \frac{\partial^2 C_O}{\partial R^2} + \frac{1}{R} \frac{\partial C_O}{\partial R} + \frac{\partial^2 C_O}{\partial Z^2}; \quad \tau > 0, 0 \leq R < \text{RS}, -L < Z < \text{LL} \quad (\text{A4.b})$$

$$C_R = 1, C_O = 0; \quad \tau = 0 \text{ (initial conditions)} \quad (\text{A5})$$

$$\frac{C_O}{C_R} = \exp \left(\frac{nF}{RT} (E - E^{o'}) \right); \\ \frac{\partial C_R}{\partial n} = -\frac{\partial C_O}{\partial n}; \quad \tau > 0, 1 - \text{TC} \leq R \leq 1, Z = 0; \\ -H \leq Z \leq 0, R = 1 - \text{TC} - Z \tan \theta \text{ (carbon surface)} \quad (\text{A6})$$

where R is the gas constant, T is the temperature, E is the electrode potential, $E^{o'}$ is the formal potential, and $\partial C(R, Z, \tau)/\partial n$ is the normal derivative.

$$\frac{\partial C_R}{\partial n} = 0, \frac{\partial C_O}{\partial n} = 0; \quad \tau > 0, Z = 0, 1 < R \leq \text{RG}; \\ -L \leq Z \leq 0, R = \text{RG} - Z \tan \theta \text{ (outer pipette wall)} \quad (\text{A7})$$

$$\begin{aligned} C_R = 1, C_O = 0; \tau > 0, Z = LL, 0 \leq R \leq RS; \\ -L \leq Z \leq LL, R = RS; \\ Z = -L, RG + L \tan \theta < R \leq RS \\ (\text{simulation space limit}) \end{aligned} \quad (\text{A8})$$

$$\frac{\partial C_R}{\partial R} = \frac{\partial C_O}{\partial R} = 0; \\ \tau > 0, R = 0, -H \leq Z \leq LL \text{ (axis of symmetry)} \quad (\text{A9})$$

In cyclic voltammetry, the potential was swept linearly at a constant scan rate v from the initial potential, E_i , and the sweep direction was reversed at the switching potential, E_s . In the dimensionless form, the potential sweep rate was expressed as the following:

$$\sigma = \frac{a^2}{4D} \frac{nFv}{RT} \quad (\text{A10})$$

The dimensionless current obtained by integrating the diffusion flux over the carbon surface corresponds to the physical current normalized by the diffusion limiting current to the inlaid disk with the radius a (eq 1).

ASSOCIATED CONTENT

Supporting Information

COMSOL Model Report. This material is available free of charge via the Internet at <http://pubs.acs.org>.

AUTHOR INFORMATION

Corresponding Authors

*M. V. Mirkin. E-mail: mmirkin@qc.cuny.edu.

*Y. Gogotsi. E-mail: gogotsi@drexel.edu.

Present Address

¹Physicochimie des Electrolytes, Colloides et Sciences Analytiques, ESPCI ParisTech, CNRS-UMR 7195, 10 rue Vauquelin, 75231 Paris Cedex 05, France.

Notes

The authors declare no competing financial interest.

ACKNOWLEDGMENTS

The support of this work by the National Science Foundation (CHE-0957313 and CHE-1026582) and the Donors of the Petroleum Research Fund administrated by the American Chemical Society is gratefully acknowledged. Carbon electrode development was supported by a Single Cell Science, Engineering and Medicine grant from Drexel University. We thank Dr. Riju Singhal for obtaining a TEM image (Figure 3).

REFERENCES

- (1) Murray, R. W. *Chem. Rev.* **2008**, *108*, 2688.
- (2) Oja, S. M.; Wood, M.; Zhang, B. *Anal. Chem.* **2013**, *85*, 473.
- (3) Ewing, A. G.; Strein, T. G.; Lau, Y. Y. *Acc. Chem. Res.* **1992**, *25*, 440.
- (4) Fasching, R. J.; Bai, S.-J.; Fabian, T.; Prinz, F. B. *Microelectron. Eng.* **2006**, *83*, 1638.
- (5) Zhan, W.; Bard, A. J. *Anal. Chem.* **2006**, *78*, 726.
- (6) Sun, P.; Laforge, F. O.; Abeyweera, T. P.; Rotenberg, S. A.; Carpino, J.; Mirkin, M. V. *Proc. Nat. Acad. Sci. U. S. A.* **2008**, *105*, 443.
- (7) Fan, F.-R. F.; Bard, A. J. *Science* **1995**, *267*, 871.
- (8) Sun, P.; Mirkin, M. V. *J. Am. Chem. Soc.* **2008**, *130*, 8241.
- (9) Lemay, S. G.; Kang, S.; Mathwig, K.; Singh, P. S. *Acc. Chem. Res.* **2013**, *46*, 369.

- (10) Schrlau, M.; Dun, N.; Bau, H. *ACS Nano* **2009**, *3*, 563.
- (11) Singhal, R.; Orynbayeva, Z.; Sundaram, R. V. K.; Niu, J. J.; Bhattacharyya, S.; Vitol, E. A.; Schrlau, M. G.; Papazoglou, E. S.; Friedman, G.; Gogotsi, Y. *Nature Nanotechnol.* **2011**, *6*, 57.
- (12) Wang, Y.; Noël, J.-M.; Velmurugan, J.; Nogala, W.; Mirkin, M. V.; Lu, C.; Guille Collignon, M.; Lemaître, F.; Amatore, C. *Proc. Natl. Acad. Sci. U. S. A.* **2012**, *109*, 11534.
- (13) Kaetelhoen, E.; Hofmann, B.; Lemay, S. G.; Zevenbergen, M. A. G.; Offenhäusser, A.; Wolfrum, B. *Anal. Chem.* **2010**, *82*, 8502.
- (14) Lizana, L.; Konkoli, Z.; Bauer, B.; Jesorka, A.; Orwar, O. *Annu. Rev. Phys. Chem.* **2009**, *60*, 449.
- (15) Clark, R. A.; Hietpas, P. B.; Ewing, A. G. *Anal. Chem.* **1997**, *69*, 259.
- (16) Laforge, F. O.; Carpino, J.; Rotenberg, S. A.; Mirkin, M. V. *Proc. Natl. Acad. Sci. U. S. A.* **2007**, *104*, 11895.
- (17) (a) Vitol, E.; Schrlau, M. G.; Bhattacharyya, S.; Ducheyne, P.; Bau, H. H.; Friedman, G.; Gogotsi, Y. *Chem. Vap. Deposition* **2009**, *15*, 204. (b) Singhal, R.; Bhattacharyya, S.; Orynbayeva, Z.; Vitol, E.; Friedman, G.; Gogotsi, Y. *Nanotechnology* **2010**, *21*, 015304. (c) Hu, K.; Gao, Y.; Wang, Y.; Yu, Y.; Zhao, X.; Rotenberg, S. A.; Gökmeşe, E.; Mirkin, M. V.; Friedman, G.; Gogotsi, Y. *J. Solid State Electrochem.* **2013**, *17*, 2971.
- (18) Wang, Y.; Kececi, K.; Velmurugan, J.; Mirkin, M. V. *Chem. Sci.* **2013**, *4*, 3606.
- (19) Sun, P.; Mirkin, M. V. *Anal. Chem.* **2006**, *78*, 6526.
- (20) (a) Shoup, D.; Szabo, A. *J. Electroanal. Chem.* **1984**, *160*, 27. (b) Zoski, C. G.; Mirkin, M. V. *Anal. Chem.* **2002**, *74*, 1986.
- (21) Hubbard, A. T.; Anson, F. C. In *Electroanalytical Chemistry*; Bard, A. J., Ed.; Marcel Dekker: New York, 1970; Vol. 4, p 129.
- (22) (a) Smythe, W. R. *J. Appl. Phys.* **1951**, *22*, 1499. (b) Szabo, A. J. *Phys. Chem.* **1987**, *91*, 3108. (c) Lee, Y.; Amemiya, S.; Bard, A. J. *Anal. Chem.* **2001**, *73*, 2261.
- (23) (a) Bond, A. M.; Luscombe, D.; Oldham, K. B.; Zoski, C. G. *J. Electroanal. Chem.* **1988**, *249*, 1. (b) Bartlett, P. N.; Taylor, S. L. *J. Electroanal. Chem.* **1998**, *453*, 49. (c) Sun, P.; Mirkin, M. V. *Anal. Chem.* **2007**, *79*, 5809.
- (24) Zhang, B.; Zhang, Y.; White, H. S. *Anal. Chem.* **2004**, *76*, 6229.
- (25) Bard, A. J.; Faulkner, L. R. *Electrochemical Methods: Fundamentals and Applications*; John Wiley & Sons, Inc.: New York, 2001, pp 239–241.
- (26) Megaridis, C. M.; Yazicioglu, A. G.; Libera, J. A.; Gogotsi, Y. *Phys. Fluids* **2002**, *14*, L5.
- (27) Mirkin, M. V.; Fan, F.-R. F.; Bard, A. J. *Science* **1992**, *257*, 364.
- (28) (a) Shao, Y.; Mirkin, M. V. *J. Phys. Chem. B* **1998**, *102*, 9915. (b) Amphlett, J. L.; Denuault, G. *J. Phys. Chem. B* **1998**, *102*, 9946.